Journal of the Brazilian Society of Mechanical Sciences and Engineering (2019) 41:470
https://doi.org/10.1007/s40430-019-1978-2

TECHNICAL PAPER

# Influence of blade profile on energy loss of sewage self-priming pump

**Denghao Wu[1,2] · Zhibing Zhu[2] · Yun Ren[3,4] · Yunqing Gu[1] · Peijian Zhou[1]**

Received: 20 July 2018 / Accepted: 21 September 2019 / Published online: 3 October 2019


**Abstract**
Sewage self-priming pumps are widely used in municipal sewage treatment and agricultural irrigation. The impeller is the key component to determine the hydraulic performance of sewage self-priming pump. In this study, the ZW100-100-15 sewage self-priming pump was selected as a research object. Five double-channel impellers with different blade profiles were designed based on the same meridional shape. The ANSYS CFX 16.2 and shear stress transport $k$–$\omega$ turbulence model were conducted to investigate the sewage pump models with five different impellers numerically. The entropy production theory was applied to analyze the internal energy losses of different sewage pump models. The mechanism of influence of blade profiles on the energy losses was investigated systematically. The results indicated that under different flow rate conditions, the hydraulic efficiency of S5 scheme with a concave blade angle distribution profile is higher than that of other schemes. At the design flow rate, the head of S5 was the highest, the flow state inside the impeller was the most stable and the energy loss inside the impeller was the least. In non-design conditions, the flow distribution and entropy production rate distribution of S5 were significantly better than those of other schemes. Results illustrated that flow separation, backflow, shock effect, vortex and rotor–stator interaction were the main inducers for the formation of entropy production. This research indicated that the entropy production theory can predict the irreversible energy loss in pump accurately and the blade profile optimization can effectively improve the sewage self-priming pump hydraulic performance and weaken the unstable flow and its internal energy loss.

**Keywords** Blade profile · Sewage self-priming pump · Entropy production · Energy loss

## 1 Introduction

With the development of "five water treatment" in China [1], as a general centrifugal pump, the sewage self-priming pump has been widely used in municipal wastewater treatment. At present, the sewage self-priming pumps are generally characterized by low efficiency and high energy consumption [2]. Therefore, it is great practical significance to improve the performance of sewage self-priming pump to reduce its energy consumption and realize the energy saving and emission reduction. As a core component of a centrifugal pump, the impeller blade profile is one of the important factors affecting the performance of a centrifugal pump, because it can change the hydraulic load on blades and affects the conversion efficiency of pressure energy in the impeller. It is known that there are many factors influencing blade profile, including blade trailing edge thickness and outlet placement angle [3–7] and blade wrap angle [8, 9]. Also the Bezier's curve method was utilized to design the blade profiles [10], or a three-dimensional blade inverse method based on free-form surface deformation method was proposed to optimize the impeller blade [11]. Recently, computational fluid dynamics (CFD) has been applied to analyze the flow fields in pump, the distribution of static pressure, fluid velocity and turbulent kinetic energy of the internal flow field of the pump which were obtained by numerical simulation [12–14]. As we know, it has some limitations for the traditional method for evaluating

Technical Editor: Jader Barbosa Jr., PhD.

✉ Yun Ren
renyun_ry@hotmail.com

[1] College of Metrology and Measurement Engineering, China Jiliang University, Hangzhou, China

[2] College of Mechanical Engineering, Zhejiang University of Technology, Hangzhou, China

[3] Zhijiang College, Zhejiang University of Technology, Shaoxing, China

[4] Faculty of Mechanical Engineering and Automation, Zhejiang Sci-Tech University, Hangzhou, China

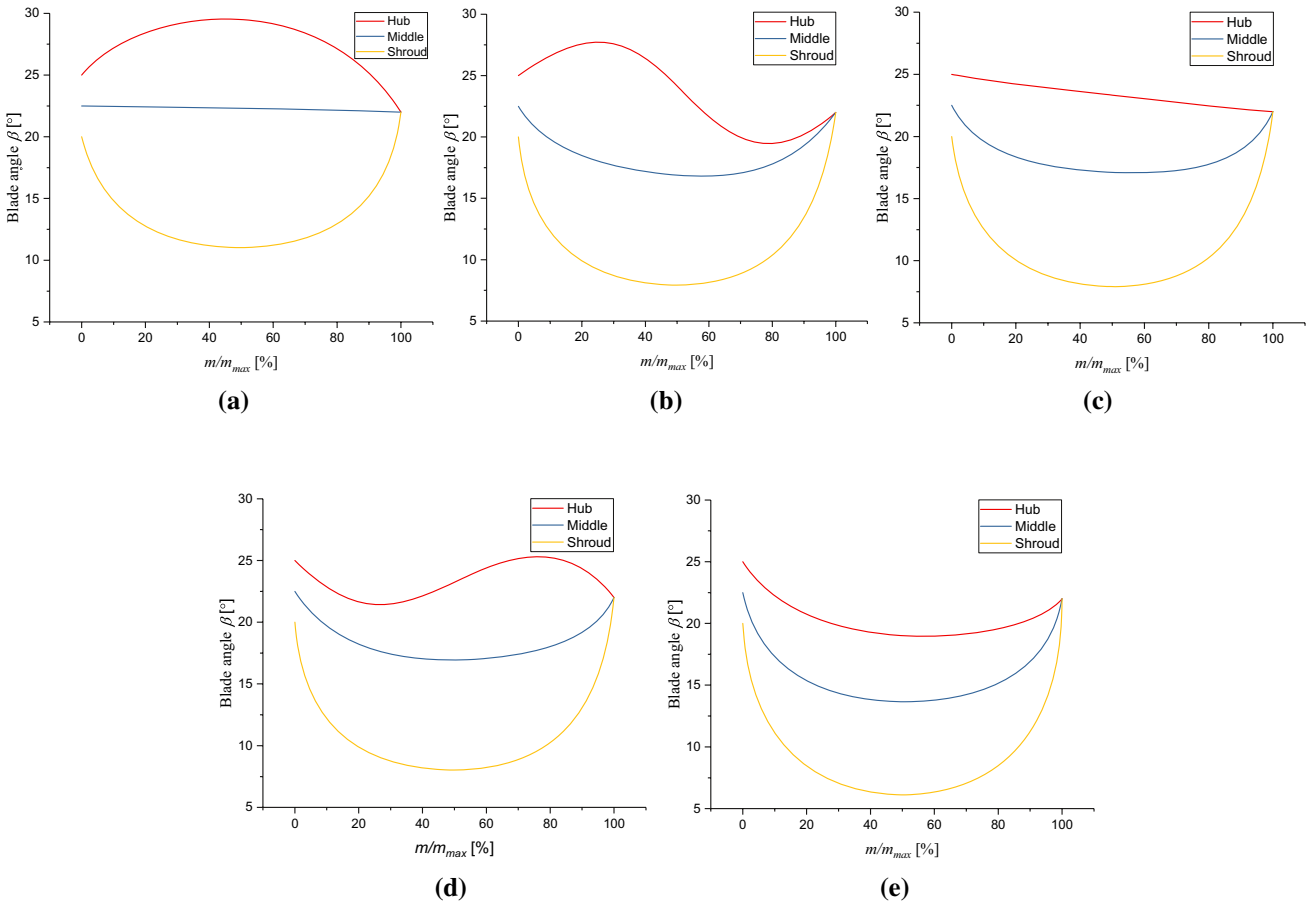


**Fig. 1** Blade placement angle distribution of five impeller schemes. **a** S1 blade, **b** S2 blade, **c** S3 blade, **d** S4 blade, **e** S5 blade

**Table 1** Wrap angle of the blade profiles for five different impeller schemes

| Impeller schemes | $\phi_{\text{Hub}}$ [°] | $\phi_{\text{Middle}}$ [°] | $\phi_{\text{Shroud}}$ [°] |
|---|---|---|---|
| S1 | 130 | 127 | 122 |
| S2 | 160 | 156 | 150 |
| S3 | 160 | 156 | 150 |
| S4 | 160 | 156 | 150 |
| S5 | 190 | 186 | 180 |

the hydraulic loss in pump based on the pressure drop. Therefore, some researchers adopted the entropy production theory to quantitatively evaluate the energy loss features inside pump and provide accurate and intuitive information for subsequent improvement and optimization for pump [15–18]. In addition, entropy production theory was also widely used in heat transfer, microscopic particle motion and other fields [19–22].

In the present study, in order to understand the influence of impeller blade profile on the performance of centrifugal pump in-depth, five different blade schemes were obtained by adjusting the hub, middle and shroud profiles of the blade. Based on the numerical method and entropy production theory, the sewage self-priming pump models under different blade schemes were studied and the flow states and energy losses inside the pump were analyzed quantitatively.

## 2 Entropy production theory

It is well known that entropy is produced in an irreversible process. Any real fluid system features entropy production phenomena under the second law of thermodynamics. The entropy production method can be used to predict the hydraulic loss of centrifugal pumps accordingly [23].

The flow state of a centrifugal pump is turbulent. Time-averaged movement and velocity fluctuation together form the turbulent flow responsible for the rate of entropy production. The entropy production rate (EPR, $\dot{S}'''$) is calculated as follows [24]:

$$\dot{S}''' = \dot{S}'''_D + \dot{S}'''_{D'} \tag{1}$$

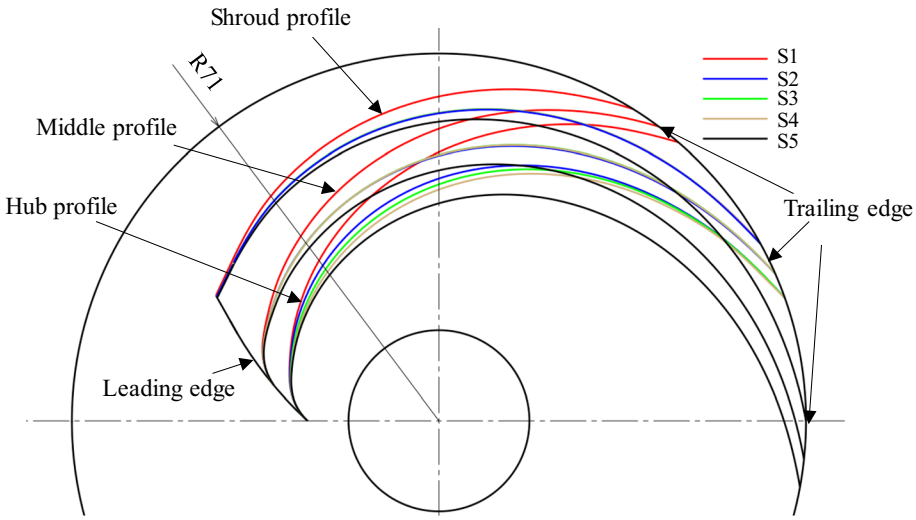


**Fig. 2** Blade shapes distribution of five impeller schemes

The time-averaged movement part is presented in Eq. (2) and the velocity fluctuation part is presented in Eq. (3):

$$\dot{S}_D''' = \frac{2\mu}{T}\left[\left(\frac{\partial \bar{u}}{\partial x}\right)^2 + \left(\frac{\partial \bar{v}}{\partial y}\right)^2 + \left(\frac{\partial \bar{w}}{\partial z}\right)^2\right] + \frac{\mu}{T}\left[\left(\frac{\partial \bar{v}}{\partial x} + \frac{\partial \bar{u}}{\partial y}\right)^2 + \left(\frac{\partial \bar{w}}{\partial x} + \frac{\partial \bar{u}}{\partial z}\right)^2 + \left(\frac{\partial \bar{v}}{\partial z} + \frac{\partial \bar{w}}{\partial y}\right)^2\right] \tag{2}$$

$$\dot{S}_{D'}''' = \frac{2\mu_{\text{eff}}}{T}\left[\left(\frac{\partial u'}{\partial x}\right)^2 + \left(\frac{\partial v'}{\partial y}\right)^2 + \left(\frac{\partial w'}{\partial z}\right)^2\right] + \frac{\mu_{\text{eff}}}{T}\left[\left(\frac{\partial v'}{\partial x} + \frac{\partial u'}{\partial y}\right)^2 + \left(\frac{\partial w'}{\partial x} + \frac{\partial u'}{\partial z}\right)^2 + \left(\frac{\partial v'}{\partial z} + \frac{\partial w'}{\partial y}\right)^2\right] \tag{3}$$

where $\dot{S}_D'''$ is the entropy production rate caused by time-averaged movement; $\dot{S}_{D'}'''$ is the entropy production rate caused by velocity fluctuation; $\mu$ is the dynamic viscosity; $\bar{u}$, $\bar{v}$ and $\bar{w}$ are the time-averaged velocity components (m/s); $u'$, $v'$ and $w'$ are the fluctuation velocity components (m/s); $T$ is the temperature; the constant value of 293 K is set for calculation; $\mu_{\text{eff}}$ is the effective dynamic viscosity and is defined in Eq. (4):

$$\mu_{\text{eff}} = \mu + \mu_{\text{t}} \tag{4}$$

in which $\mu_{\text{t}}$ is the turbulent dynamic viscosity (Pa s).

$\dot{S}_D'''$ can be calculated directly by simulation; however, the $\dot{S}_{D'}'''$ is not calculated directly; instead, it can be calculated as follows [25]:

$$\dot{S}_{D'}''' = \alpha\frac{\rho\omega k}{T} \tag{5}$$

where $\alpha = 0.09$, $\omega$ is the turbulent eddy frequency ($s^{-1}$) and $k$ is the turbulent energy ($m^2/s^2$).

The total EPR $S_{\text{pro}}$ is an integration of the local EPR volumes:

$$S_{\text{pro}} = \int_V \dot{S}_D'''\mathrm{d}V + \int_V \dot{S}_{D'}'''\mathrm{d}V \tag{6}$$

where $V$ is the volume of flow passage in each hydraulic component.

## 3 Calculation model and calculation method

### 3.1 Basic parameters of model pump

In the present study, a ZW100-100-15 sewage self-priming pump was employed as the research object. The design parameters of pump are flow rate $Q_{\text{d}} = 100$ $m^3/h$, head $H_{\text{d}} = 15$ m, speed $n = 2900$ r/min, inlet diameter $D_1 = 98$ mm, outlet diameter $D_2 = 142$ mm, number of blades $Z = 2$ and blade outlet height $b_2 = 68$ mm. The inlet and outlet placement angle of blade profile on shroud surface is $\beta_{1\text{s}} = 20°$ and $\beta_{2\text{s}} = 22°$, respectively; the inlet and outlet placement angle of blade profile on middle surface is $\beta_{1\text{m}} = 22.5°$ and $\beta_{2\text{m}} = 22°$, respectively; the inlet and outlet placement angle of blade profile on hub surface is $\beta_{1\text{h}} = 25°$ and $\beta_{2\text{h}} = 22°$. In addition, the blade inlet thickness is 5 mm and the outlet thickness is 6 mm.

Figure 1 shows the blade placement angle profiles for different impellers in which the blade angle distribution profile on hub surface of S1, S2, S3, S4 and S5 was arranged in a convex shape, a saddle shape, a linear drop shape, an inverse saddle shape and a concave shape, respectively. The shroud profile and the middle profile were adjusted according to the shape of hub profile by the Bezier control points automatically, and the blade wrap angle of each scheme also changes accordingly.

Table 1 shows the wrap angle of the blade profiles for five different impeller schemes. Moreover, the shapes of

**Table 2** Blade radius distribution of five impeller schemes

| $\varphi$ (°) | S1 | | | S2 | | | S3 | | | S4 | | | S5 | | |
|---|---|---|---|---|---|---|---|---|---|---|---|---|---|---|---|
| | $R_h$ (mm) | $R_m$ (mm) | $R_s$ (mm) | $R_h$ (mm) | $R_m$ (mm) | $R_s$ (mm) | $R_h$ (mm) | $R_m$ (mm) | $R_s$ (mm) | $R_h$ (mm) | $R_m$ (mm) | $R_s$ (mm) | $R_h$ (mm) | $R_m$ (mm) | $R_s$ (mm) |
| 0 | 25.4 | | | 25.4 | | | 25.4 | | | 25.4 | | | 25.4 | | |
| 10 | 28.89 | 12°/32.6 | | 28.86 | 12°/32.6 | | 28.8 | 12°/32.6 | | 28.76 | 12°/32.6 | | 28.73 | 12°/32.6 | |
| 20 | 30.75 | 36.26 | 25°/44.15 | 30.64 | 36.16 | 25°/44.15 | 30.46 | 36.14 | 25°/44.15 | 30.34 | 36.15 | 25°/44.15 | 30.24 | 36.05 | 25°/44.15 |
| 40 | 35.09 | 41.03 | 51.04 | 34.54 | 40.21 | 50.56 | 33.93 | 40.16 | 50.59 | 33.53 | 40.16 | 50.56 | 33.14 | 39.56 | 50.31 |
| 60 | 40.81 | 46.61 | 55.85 | 39.13 | 44.4 | 54.38 | 38.1 | 44.39 | 54.45 | 37.36 | 44.38 | 54.38 | 36.39 | 42.99 | 53.64 |
| 80 | 47.91 | 53 | 60.41 | 44.19 | 48.89 | 57.79 | 43.01 | 48.99 | 57.89 | 42.03 | 48.98 | 57.82 | 40.06 | 46.58 | 56.48 |
| 100 | 56.27 | 60.1 | 65.03 | 49.63 | 53.72 | 61.05 | 48.67 | 53.92 | 61.16 | 47.67 | 53.9 | 61.11 | 44.19 | 50.33 | 59.05 |
| 120 | 65.62 | 68.02 | 70.38 | 55.61 | 58.98 | 64.4 | 55.06 | 59.24 | 64.49 | 54.29 | 59.19 | 64.49 | 48.81 | 54.28 | 61.61 |
| 130 | 71 | 127°/71 | 122°/71 | 58.9 | 61.84 | 66.21 | 58.55 | 62.1 | 66.29 | 57.96 | 62.05 | 66.31 | 51.32 | 56.35 | 62.9 |
| 140 | | | | 62.44 | 64.95 | 68.22 | 62.29 | 65.16 | 68.28 | 61.89 | 65.13 | 68.32 | 53.99 | 58.52 | 64.23 |
| 150 | | | | 66.35 | 68.43 | 71 | 66.32 | 68.56 | 71 | 66.12 | 68.53 | 71 | 56.82 | 60.8 | 65.65 |
| 160 | | | | 71 | 156°/71 | | 71 | 156°/71 | | 71 | 156°/71 | | 59.86 | 63.24 | 67.19 |
| 170 | | | | | | | | | | | | | 63.14 | 65.93 | 68.93 |
| 180 | | | | | | | | | | | | | 66.74 | 68.94 | 71 |
| 190 | | | | | | | | | | | | | 71 | 186°/71 | |

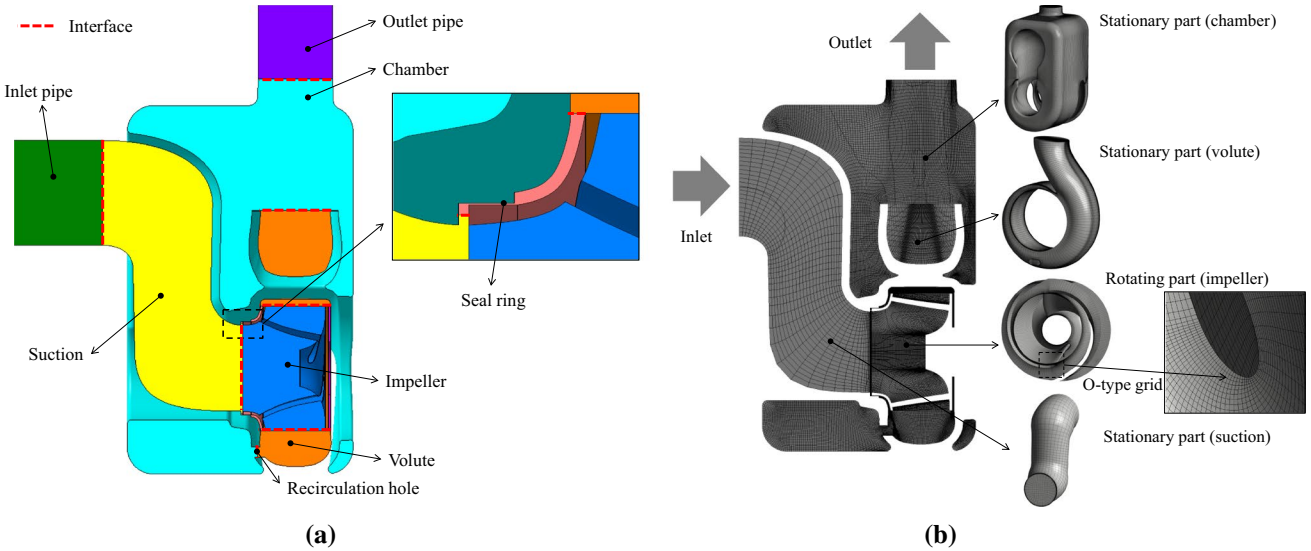


**Fig. 3** Computational domains of a pump model. **a** Fluid domains, **b** calculation meshes

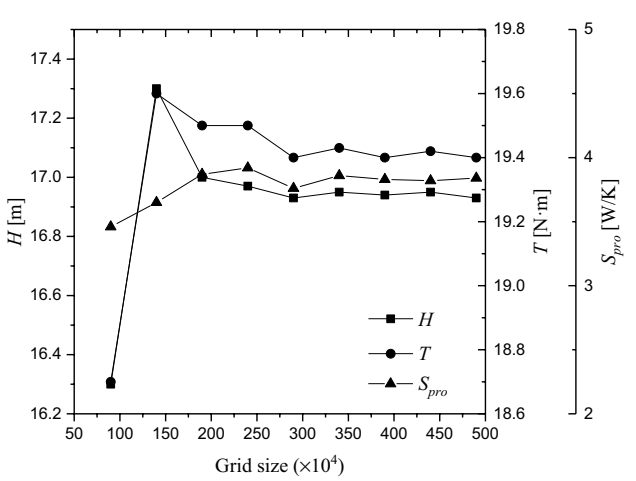


**Fig. 4** Grid sensitivity validation ($1.0Q_d$)

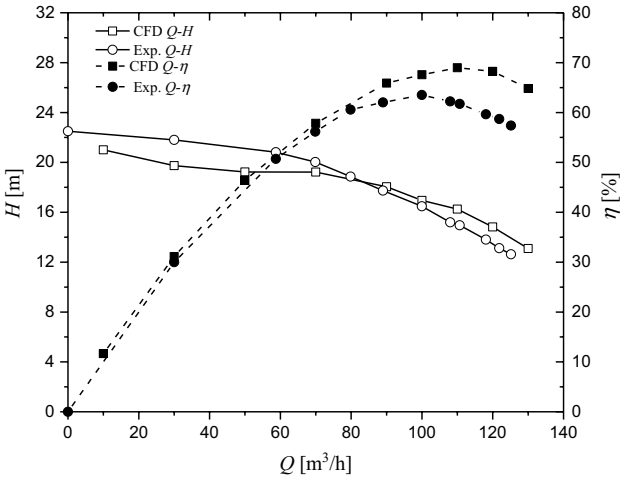


**Fig. 5** Validation for performance data of S5

blade without thickness of five different impeller schemes are presented in Fig. 2. And the detail information of blade radius distributions of five impeller schemes is given in Table 2.

## 3.2 Fluid domains and mesh

The fluid domains of pump included the inlet pipe, suction, impeller, volute, chamber, outlet pipe, seal ring and recirculation hole (Fig. 3a). The leakage flow effect on hydraulic performance was considered by involving the seal ring during the modeling process. The lengths of inlet pipe and outlet pipe were set as ten times of the pipe diameter. The fluid domains of pump were constructed by 3D software and meshed into hexahedral grids by using commercial software GridPro (Fig. 3b). The blades and tongue were well refined to keep high mesh quality. Taking S5 as an example, the grid sensitivity test was performed by ANSYS CFX with SST $k$–$\omega$ turbulence model. The grid sensitivity analysis was carried out to determine the appropriate number of grids. Figure 4 shows that as the number of grid is about 3.9 million, the head ($H$), torque ($T$) and total entropy production rate ($S_{pro}$) basically remain stable and their value is about 16.9 m, 19.4 N m and 3.8 W/K, respectively, under designed flow rate condition. In order to balance the calculation accuracy and calculation time, the total mesh number of the final model is set at 3,931,964, in which the number of grids of impeller, volute, chamber and suction is 555,532, 461,312,

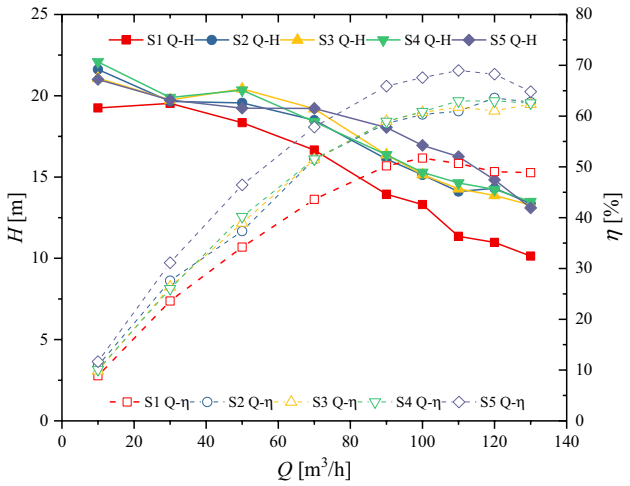


**Fig. 6** Performance curves of five different impellers under different flow rate conditions

2,157,056 and 170,000, respectively, and the grid number of other computing domains is 588,064.

### 3.3 Numerical approach

Performance data and flow fields of the sewage self-priming pump were calculated numerically. The SST $k$–$\omega$ turbulence model was applied to solve the calculation. The boundary condition was set as the total pressure inlet and its relative pressure was 0 bar, and the outlet was set as the mass flow outlet. The wall of the fluid domain was divided into two types: rough wall surface and smooth wall surface. The impeller and pump casing were made by sand casting process; therefore, those were set as no-slip rough surfaces with a roughness of 0.04 mm, while the other parts were set as no-slip smooth walls. The rotating and static couplings of the interface between the impeller and the suction, and the interface between the impeller and the volute were set as the frozen rotor interface. Since both sides of the interface have disconnected meshes and nodes, the general grid interface was applied to transfer information from one side to another. The high-order solution was set for calculation with the convergence residual RMS below $10^{-5}$ for all equations.

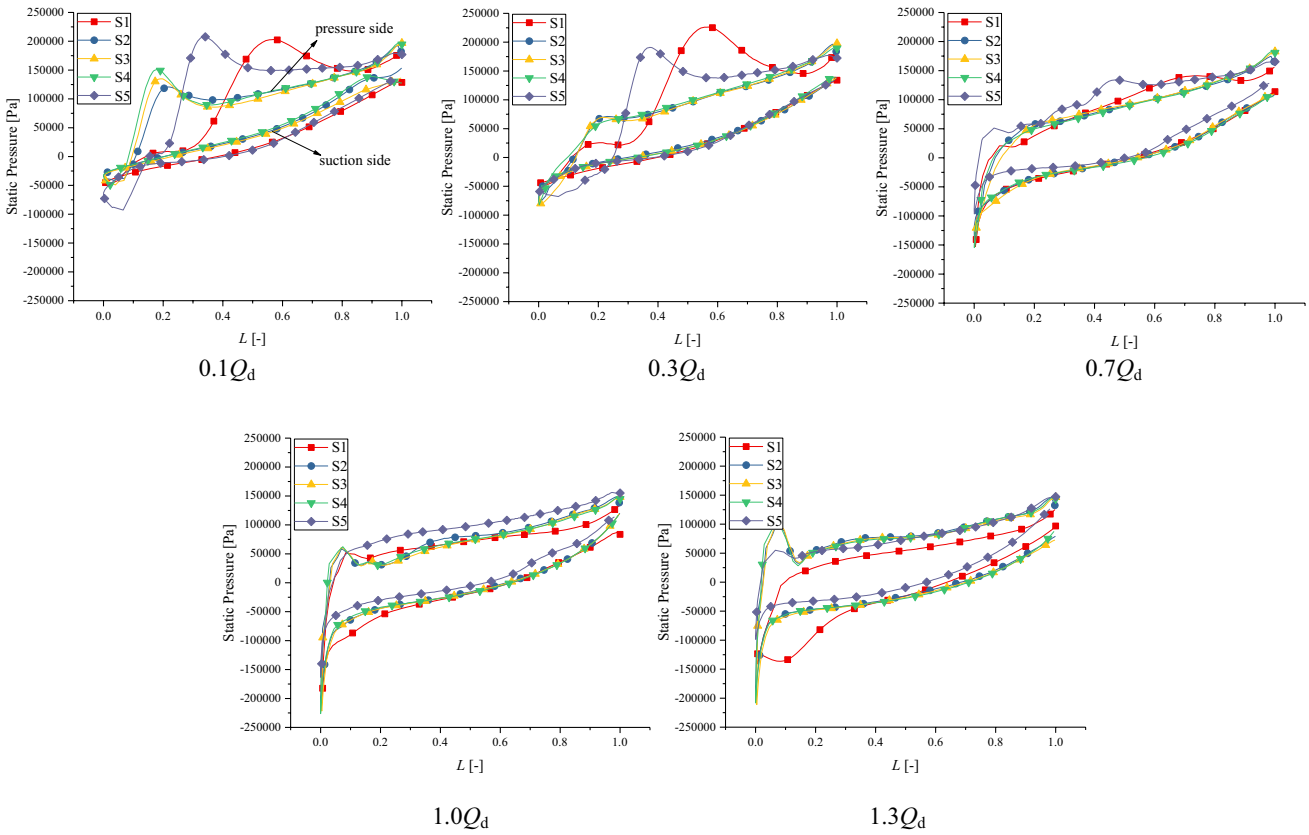


**Fig. 7** Static pressure loads of five different impellers at span 0.5 under different flow rate conditions

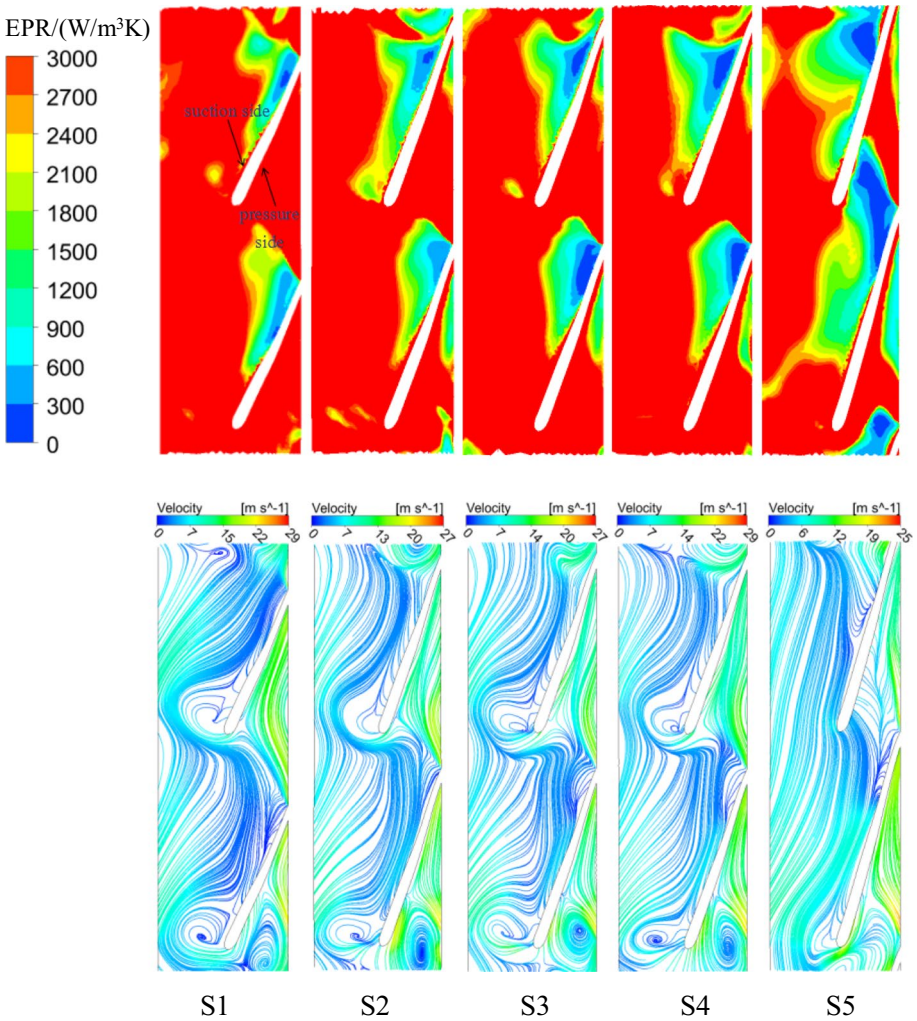


**Fig. 8** EPR distribution and streamlines at middle-span surface of different impellers at $0.1Q_d$

### 3.4 Validation of numerical method

Figure 5 shows the performance curve comparison between the experimental results and the numerical results of S5. As can be seen from the figure, the maximum deviation of head under the part-load conditions is about 8%. It is because the existing numerical method is incapable to predict pump performance accurately at small flow rate conditions for the high complex turbulent flows inside pump. At the designed flow rate $Q_d = 100$ m$^3$/h, the calculated head is 16.9 m, while the experimental head is 16.58 m. Therefore, its error is 0.32 m, and the relative error is 1.93%, which meets the calculation accuracy requirements. As the flow rate moves to the over-load conditions, the head error slightly increases. Furthermore, as for the efficiency curve, the consistency between the experimental value and the calculated value is relative well. However, at high flow rate conditions, there is a certain deviation between the two. It is due to the mechanical and leakage losses which are not considered in the efficiency calculation. Based on the above analysis, the numerical calculation model has better accuracy and can meet the following calculation and verification requirements.

## 4 Results and discussion

### 4.1 Performance curves of different blade profiles

Figure 6 shows the hydraulic performance calculation results for the sewage self-priming pump models with five different impellers.

It is obviously found that the relative difference among the performance curves of S2, S3 and S4 is small. Looking at the $Q$–$H$ curve only, the head of S1 is the lowest at any flow rate, and a local hump phenomenon occurs in the small flow rates area. As the flow rate increases up to the design and overflow operating points, the head value of S5 is higher than that of the others. In addition, as for the S5, the head at the design flow rate of 100 m$^3$/h is 16.9 m, which is higher than the target design head and the head of

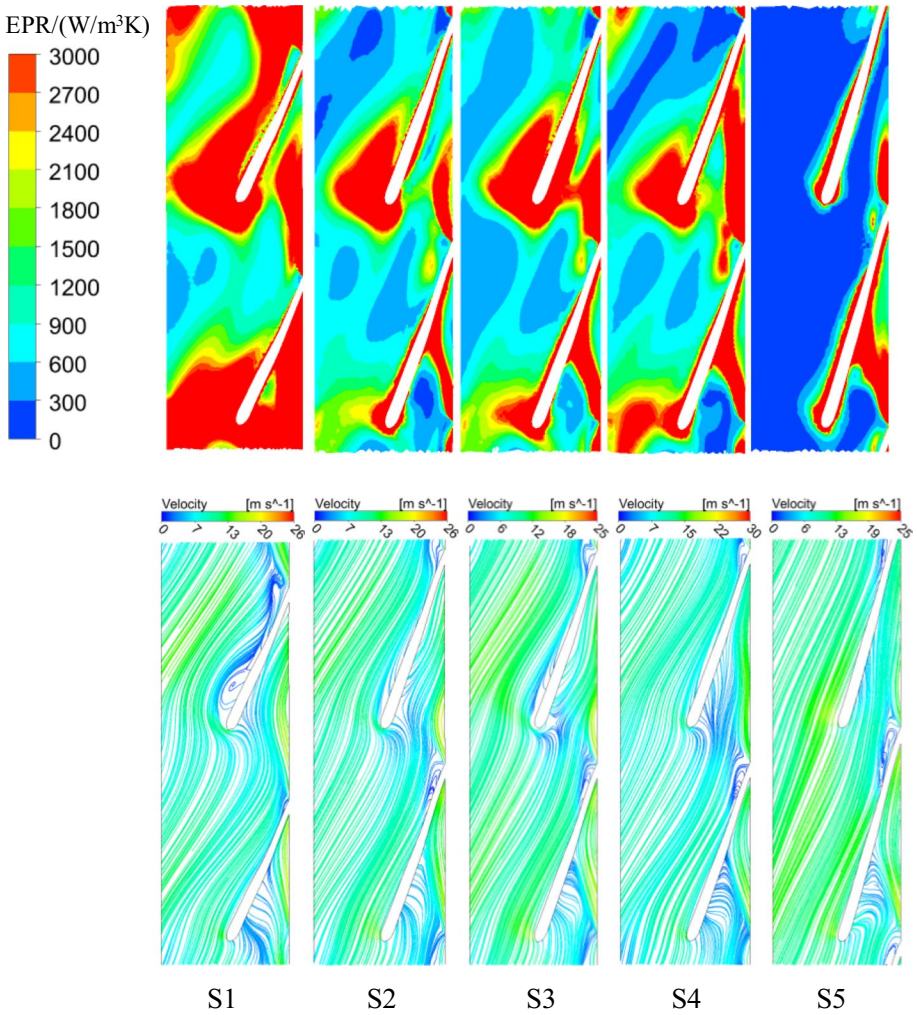


**Fig. 9** EPR distribution and streamlines at middle-span surface of different impellers at $0.7Q_d$

S2, S3 and S4 basically meets the target, while the S1 has a low head at design flow rate and fails to meet the target. Furthermore, for the $Q$–$\eta$ curve, it is observed that at any flow rate, the efficiency of S5 is higher than that of the others, while the efficiency of S1 is the lowest. At the design flow rate, the maximum efficiency of S5 is 67.57%, the maximum efficiency of S2, S3 and S4 is relatively close, which is 59.05%, 59.45% and 59.61%, respectively, and the efficiency of S1 is smallest whose value is 50.68%. Therefore, it can be concluded that the blade profile has a greater influence on pump performance. It is noted that the blade of S5 has a large wrap angle, which takes a good government on the fluid inside the impeller in the purpose of reducing the scale of flow slip and flow separation phenomenon greatly. It is therefore the mechanical energy can be largely converted into the potential energy. In the other hand, the blade of S1 has a smaller wrap angle, so the fluid is not controlled well in the channels, and the slip and flow separation phenomena are easier to generate. Therefore, as for S1, a high energy loss is generated and its head and efficiency are relatively low.

## 4.2 Blade loads of different blade profiles

Figure 7 shows the static pressure load curves of five different impellers at middle-span surface (span 0.5). The abscissa indicates the normalization distance from the inlet to the outlet of blade, and the ordinate indicates the static pressure load of blade. The upper curve illustrates the pressure load of the pressure side of blade, and the lower curve presents the pressure load of the suction side of blade.

It is illustrated that the static pressure loads on the blade gradually increase from the leading edge of blade to the trailing edge of blade. However, in the flow conditions of $0.1Q_d$ and $0.3Q_d$, it is obviously found that, for S1 impeller, a peak pressure value appeared at middle of pressure side of blade, which is because a large blade placement angle is given for S1 at mid-length of blade. The static pressure distribution curves of the S2, S3 and S4 impellers are basically consistent and relatively stable. With the continuous increase in flow rate, the static pressure loads of the impellers tend to be stable and evenly distributed. It can be seen clearly from the curves that the static pressure value of the pressure surface

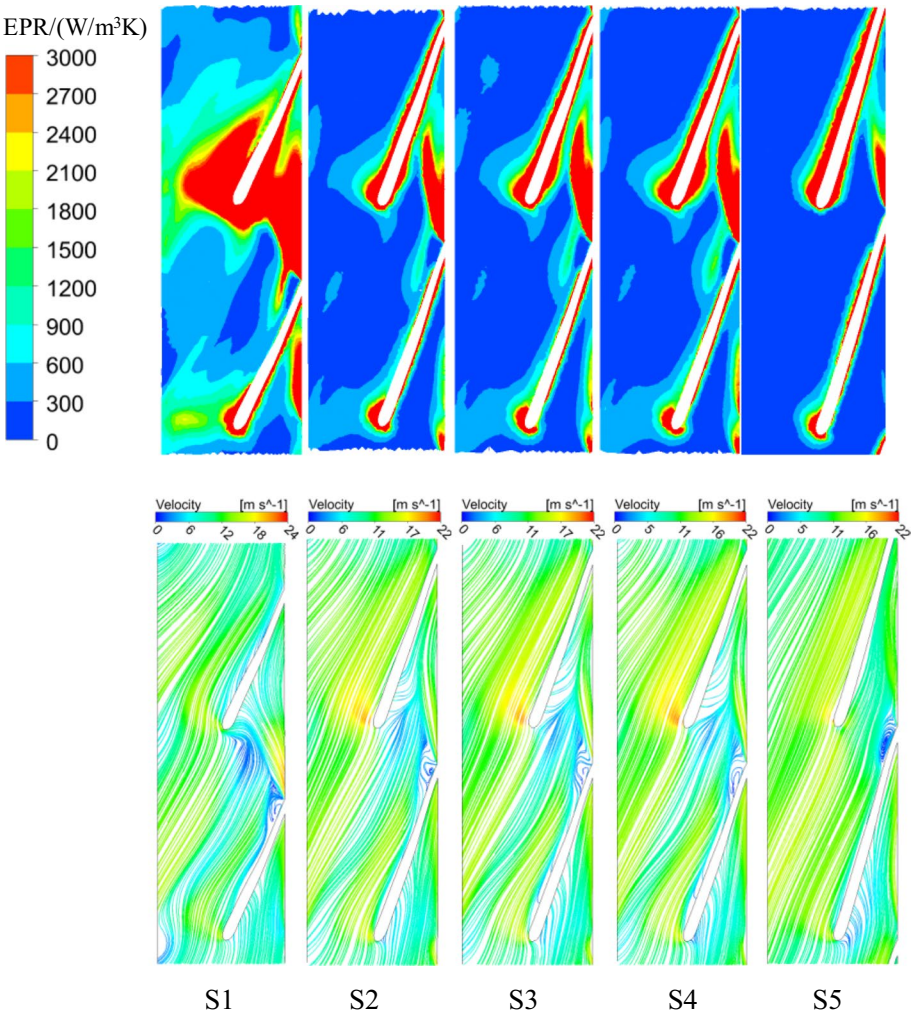


**Fig. 10** EPR distribution and streamlines at middle-span surface of different impellers at $1.0Q_d$

on the blade is basically higher than that of the suction surface, and only in the case of too low flow rates, the static pressure value of pressure side is lower than the value of the suction side appearing in a small area near the leading edge of the blade. This results from high incidence angle of flow at part-load conditions, because the high incidence angle makes the flow velocity near the pressure side of leading edge is higher that of suction side. By following the Bernoulli's principle, it determines higher pressure near suction side of blade leading edge. From the above discussion, it is concluded that the blade profile significantly influenced the flow state and pressure distribution of impeller. In addition, it is illustrated that the pressure load of the impeller at design flow rate condition is more stable than that of the non-design conditions.

### 4.3 Internal flow features of impellers with different blade profiles

Figures 8, 9, 10 and 11 show the EPR distribution and velocity streamlines of the impeller with different blade profiles on the middle-span surface (span 0.5) under four typical flow conditions. It is observed that when $Q = 0.1Q_d$, large flow separation and low-speed vortex zones are generated close to the suction side of the impellers and high energy losses are produced. This is due to the high angle of incidence of flow for a too low flow rate condition. In such a flow condition, the relative flow angle is smaller than the blade inlet placement angle, and the fluid enters the impeller as a positive incidence angle, so that the fluid velocity at the suction side of the blade is lower than that of at the middle flow across channel. The flow velocity difference enlarges the shear effect and produces the flow separation and vortex. However, as the flow rate increases, the relative flow angle is increasing and the incidence angle is decreasing; as a result, these two angles are matched, so that it makes the flow state more stable. Meanwhile, the low-speed vortex areas are also reduced significantly. At the operating points of $1.0Q_d$ and $1.3Q_d$, it can be seen that the flow angle is basically the same as the blade inlet placement angle, so that the flow entering into the blade is quite stable. There is only a local small

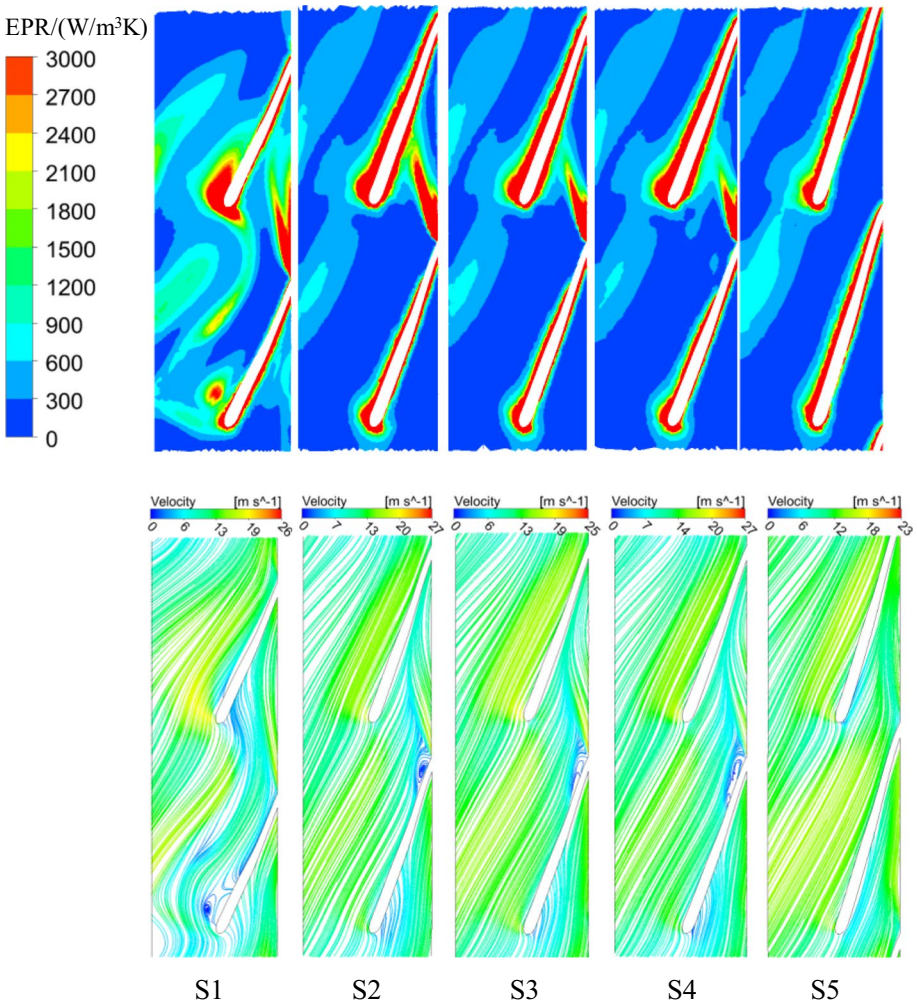


**Fig. 11** EPR distribution and streamlines at middle-span surface of different impellers at $1.3Q_d$

vortex area found at the outlet of blade, and the local energy losses are reduced more.

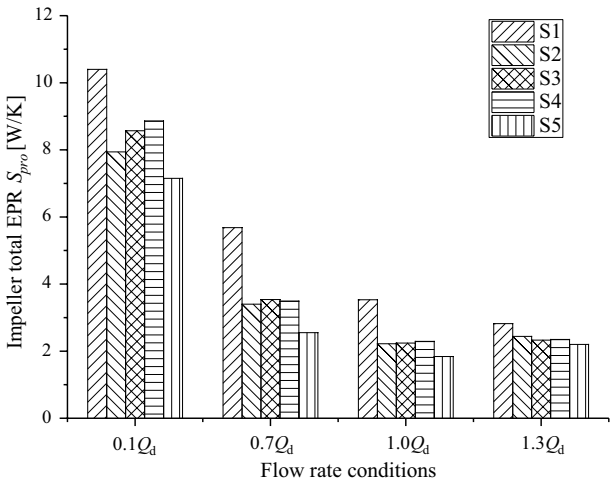


**Fig. 12** Total EPR distributions of different impellers

Figure 12 shows the total EPR ($S_{pro}$) of the impellers with different blade profiles under four typical flow conditions. It can be obtained that total EPR of S1 impeller is higher than that of other impellers and its maximum value is about 10.5 W/K at $0.1Q_d$. However, S5 impeller has minimum total EPR values and its minimum value is 1.84 W/K at $1.0Q_d$. With the increase in the flow rate, the total EPR of impeller, except S1 impeller, decreases first and then increases slightly and reaches the minimum at $1.0Q_d$. Based on the above analysis, it is presented that the flow state of the S5 impeller is the most stable and strength of vortex is the weakest; therefore, its total EPR and internal energy loss are the smallest.

### 4.4 Energy losses of pump with different blade profiles

Figures 13, 14, 15 and 16 illustrate EPR distribution of pumps with five different impellers under different flow conditions. It is presented that under part-load flow conditions, high EPR values are mainly concentrated on impeller, volute and suction areas and the less energy losses are found

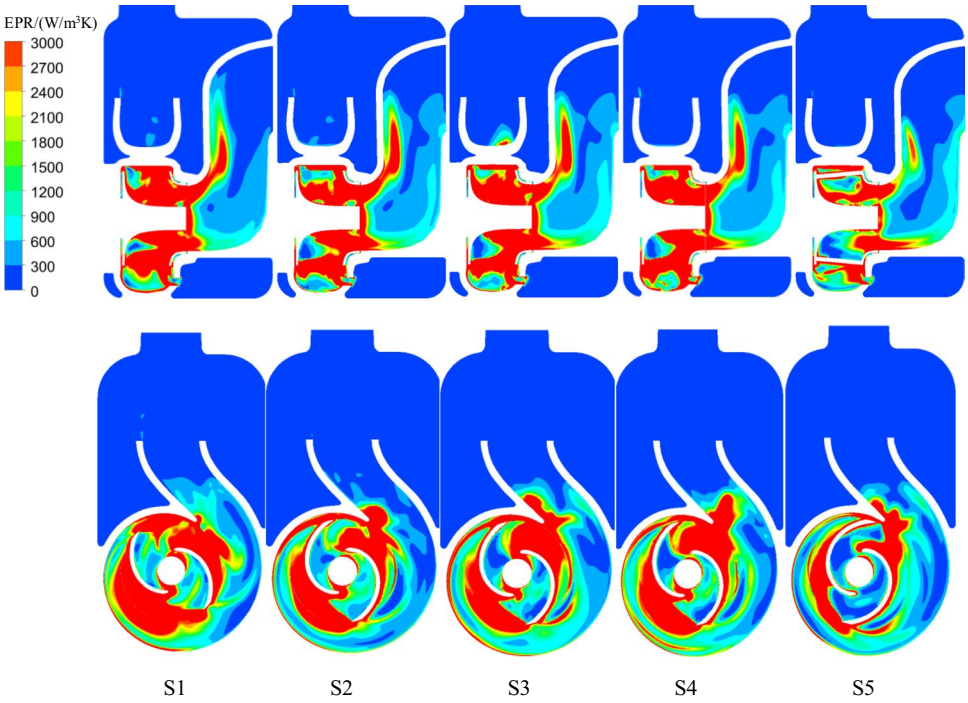


**Fig. 13** Total EPR distribution in the pump with different impellers at $0.1Q_d$

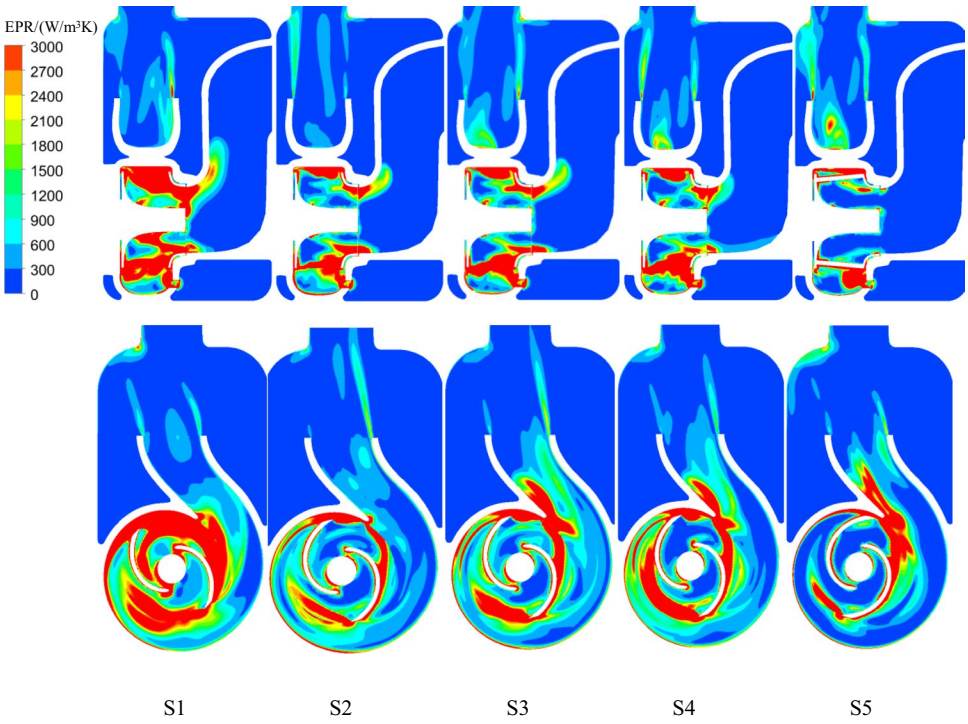


**Fig. 14** Total EPR distribution in the pump with different impellers at $0.7Q_d$

in chamber area. This is quite expected outcome, as a result of the strong hydraulic and impact losses, which induced from the backflow, flow separation, vortex and rotor–stator interactions in these flow domains. When the flow rate increases, the EPR values reduce largely and the hydraulic loss inside the impeller is significantly decreased. For the volute area, the energy loss is transferred to the diffusion section of volute, and the high EPR values appear at the upper part of the chamber. At the design and over-load flow conditions, high EPR values are observed in the impeller

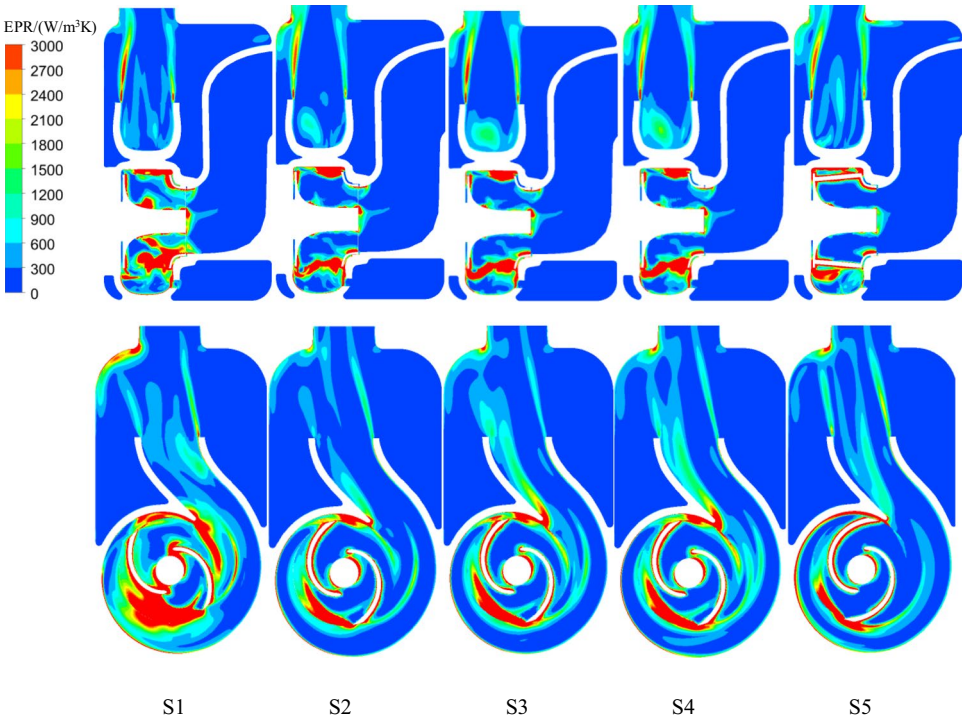


**Fig. 15** Total EPR distribution in the pump with different impellers at $1.0Q_d$

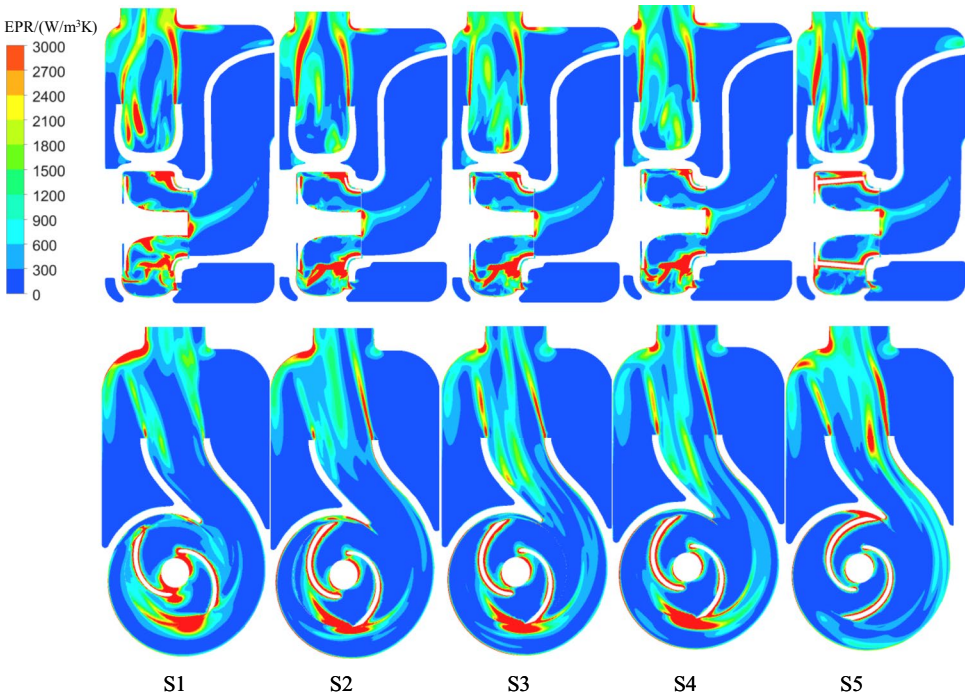


**Fig. 16** Total EPR distribution in the pump with different impellers at $1.3Q_d$

outlet, and this energy loss is mainly caused by the shearing effect between the blade trailing edge and fluid. In addition, high EPR values are also found in the volute tongue area, the diffusion section and the upper left area of the chamber. This is due to the fact that, as the flow rate increases, the high-speed jet flows pumping out from the impeller and volute enhance the shear and impact losses inside the pump.

Comparing the EPR distribution of different impeller schemes at the same flow rate condition, it is illustrated that the EPR values of S5 are lower than those of other schemes,

which indicates that the internal energy loss of S5 is the smallest and the hydraulic efficiency is the highest.

## 5 Conclusions

Based on the numerical calculation and entropy production theory, this paper investigated the internal flow characteristics and loss mechanism of a sewage self-priming pump with five different blade profile impellers. The following conclusions were obtained:

In comparison with the other blade profile impellers, it was found that the S5 impeller with the concave blade angle profile had the most stable internal flow and the lowest total EPR values. The blade with a larger blade wrap angle effectively governed the flow inside the impeller, which made the flow in the impeller channels not easy to slip and separate. Eventually, it weakened the energy losses caused by the slip and separation phenomena inside pump.

The relative flow angle of fluid inside the impeller was controlled by blade profiles. Unsuitable blade profile led to the occurrence of negative incidence angle of fluid flow in the impeller, which enlarged the impact loss and the shearing action between the fluids. And the local vortex appeared in the inlet area of the blade. Therefore, the blade profiles could determine the flow states, pressure loads and hydraulic losses of the impeller.

The entropy production theory was used to deeply analyze the distribution of energy loss inside pump with different impellers. Under small flow rate conditions, the large shear and impact effects were caused by the interferences between the high-speed jet flow from the outlet of the blade and the low-speed fluid inside the volute. The rotor and stator interactions of the impeller and volute strengthened the energy loss inside the impeller and volute. With the increase in the flow rate, the internal energy loss of the impeller was significantly reduced, and the energy loss was transferred to the diffusion section of the volute and the upper part of the chamber. This was due to the high-speed jet flows pumping out from the impeller and volute enhanced the shear and impact losses inside the volute and chamber.

**Acknowledgements** The authors gratefully acknowledge the support from the National Natural Science Foundation of China (No. 51606167 and 51609212), the Open Foundation of Zhejiang Provincial Top Key Academic Discipline of Mechanical Engineering (No. ZSTUME02A04) and Postdoctoral Research Foundation of Zhejiang Province (CN) titled with "Studies on the inner flow mechanism in the centrifugal pump impeller at lower flow rate conditions based on anisotropic LES analysis."

## References

1. Huang Y, Liu Y, Xu MZ, Zhao LQ (2016) Experience and revelation from five water body administrative management mechanism in Zhejiang Province. Environ Sci Manag 41(4):12–15 **(In Chinese)**
2. Tan LW, Zhang DS, Shi WD, Zhou L, Cai XT (2017) Influence of volute basic circle diameter on the pressure fluctuations and flow noise of a low specific speed sewage pump. J Vibroeng 19(5):3779–3796
3. Tao Y, Yuan SQ, Liu JR, Zhang F, Yuan JP (2016) Influence of blade thickness on transient flow characteristics of centrifugal slurry pump with semi-open impeller. Chin J Mech Eng 29(6):1209–1217
4. Ding HC, Li ZK, Gong XB, Li MS (2019) The influence of blade outlet angle on the performance of centrifugal pump with high specific speed. Vacuum 159:239–246
5. Yousefi H, Noorollahi Y, Tahani M, Fahimi R, Saremian S (2019) Numerical simulation for obtaining optimal impeller's blade parameters of a centrifugal pump for high-viscosity fluid pumping. Sustain Energy Technol Assess 34:16–26
6. Wang T, Kong FY, Xia B, Bai YX, Wang C (2017) The method for determining blade inlet angle of special impeller using in turbine mode of centrifugal pump as turbine. Renew Energy 109:518–528
7. Cui BL, Wang CF, Zhu ZC, Jin YZ (2013) Influence of blade outlet angle on performance of low-specific-speed centrifugal pump. J Therm Sci 22(2):117–122
8. Bai YX, Kong FY, Yang SS, Chen K, Dai T (2017) Effect of blade wrap angle in hydraulic turbine with forward-curved blades. Int J Hydrog Energy 42(29):18709–18717
9. Tan L, Zhu BS, Cao SL, Bing H, Wang YM (2014) Influence of blade wrap angle on centrifugal pump performance by numerical and experimental study. Chin J Mech Eng 27(1):171–177
10. Alexeev RA, Tishchenko VA, Gribin VG, Gavrilov IY (2017) Turbine blade profile design method based on Bezier curves. J Phys Conf Ser 891(1):1–6
11. Kruyt NP, Westra RW (2014) On the inverse problem of blade design for centrifugal pumps and fans. Inverse Probl 30(6):1–22
12. Wu DH, Ren Y, Mou JG, Gu YQ, Jiang LF (2019) Unsteady flow and structural behaviors of centrifugal pump under cavitation conditions. Chin J Mech Eng 32(1):1–15
13. Bastos HMC, Torres PJG, Álvarez CEC (2018) Numerical simulation and experimental validation of a solar-assisted heat pump system for heating residential water. Int J Refrig 86:28–39
14. Zhou L, Bai L, Li W, Shi WD, Wang C (2018) PIV validation of different turbulence models used for numerical simulation of a centrifugal pump diffuser. Eng Comput 35(1):2–17
15. Yang J, Pavesi G, Liu XH, Xie T, Liu J (2018) Unsteady flow characteristics regarding hump instability in the first stage of a multistage pump-turbine in pump mode. Renew Energy 127:377–385
16. Li DY, Wang HJ, Qin YL, Han L, Wei XZ, Qin DQ (2017) Entropy production analysis of hysteresis characteristic of a pump-turbine model. Energy Convers Manag 149:175–191
17. Li XJ, Zhu ZC, Li Y, Chen XP (2016) Experimental and numerical investigations of head-flow curve instability of a single-stage centrifugal pump with volute casing. Proc Inst Mech Eng Part A J Power Energy 230(7):633–647
18. Hou HC, Zhang YX, Li ZL, Jiang T, Zhang JY, Xu C (2016) Numerical analysis of entropy production on a LNG cryogenic submerged pump. J Nat Gas Sci Eng Part A 36:87–96
19. Blaise M, Feidt M, Maillet D (2018) Influence of the working fluid properties on optimized power of an irreversible finite dimensions Carnot engine. Energy Convers Manag 163:444–456

20. Hagerstrom AM, Murphy TE, Roy R (2015) Harvesting entropy and quantifying the transition from noise to chaos in a photon-counting feedback loop. Proc Natl Acad Sci USA 112(30):9258–9263
21. Prasad RK, Sahu MK (2017) Entropy generation and thermodynamic analysis of solar air heaters with artificial roughness on absorber plate. Arch Thermodyn 38(3):23–48
22. Gorla RSR, Gireesha BJ (2015) Transient velocity and steady state entropy generation in a microfluidic Couette flow containing charged nano particles. Int J Appl Mech Eng 20(4):787–804
23. Ren Y, Zhu ZC, Wu DH, Li XJ (2019) Influence of guide ring on energy loss in a multistage centrifugal pump. J Fluids Eng 141(6):061302
24. Bejan A (1996) Entropy generation minimization: the new thermodynamics of finite-size devices and finite-time processes. J Appl Phys 79(3):1191–1218
25. Kock F, Herwig H (2004) Local entropy production in turbulent shear flows: a high-Reynolds number model with wall functions. Int J Heat Mass Transf 47(10):2205–2215